AGU PUBLICATIONS

JGR

Journal of Geophysical Research: Oceans

RESEARCH ARTICLE
10.1002/2013JC009556

Key Points:
- Fresh surface water accumulates along coast due to on-shore Ekman transport
- Surface water spreads beneath ice shelves in a regime of coastal downwelling
- Balance between Ekman and eddy overturnings determines the downwelling depth

Correspondence to:
Q. Zhou,
zhouqin007@hotmail.com

Citation:
Zhou, Q., T. Hattermann, O. A. Nøst, M. Biuw, K. M. Kovacs, and C. Lydersen (2014), Wind-driven spreading of fresh surface water beneath ice shelves in the Eastern Weddell Sea, *J. Geophys. Res. Oceans*, *119*, 3818–3833, doi:10.1002/2013JC009556.

Received 6 NOV 2013
Accepted 13 MAY 2014
Accepted article online 17 MAY 2014
Published online 18 JUN 2014

Wind-driven spreading of fresh surface water beneath ice shelves in the Eastern Weddell Sea

Q. Zhou[1], T. Hattermann[1,2], O. A. Nøst[1,2], M. Biuw[2,3], K. M. Kovacs[1], and C. Lydersen[1]

[1]Norwegian Polar Institute, Fram Centre, Tromsø, Norway, [2]Akvaplan-niva AS, Fram Centre, Tromsø, Norway, [3]Norsk institutt for naturforskning, Fram Centre, Tromsø, Norway

Abstract Solar heated, fresh Antarctic Surface Water (ASW) is a permanent feature along the Eastern Weddell Sea (EWS) coast in summer down to a depth of roughly 200 m. Recently, ASW has been observed beneath the Fimbul Ice Shelf, suggesting that it might play an important role in basal melting. We propose that wind-driven coastal downwelling is the main mechanism that spreads ASW beneath the ice shelf in this sector of Antarctica. We validate this hypothesis with observations, scaling analyses, and numerical modeling, along three principle lines: (i) data analyses of about 1500 salinity profiles collected by instrumented seals indicate that the observed freshening of the coastal water column is likely explained by the on-shore Ekman transport and subsequent downwelling of ASW; (ii) an analytical model of the coastal momentum balance indicates that wind-driven downwelling is capable of depressing the buoyant surface water to a depth similar to the ice shelf draft; and (iii) simulations from both idealized and regional eddy-resolving numerical ice shelf/ocean models support our proposition. Our main conclusion is that wind-driven spreading of ASW beneath the ice shelf occurs when downwelling exceeds the depth of the ice shelf base. Furthermore, our study adds to the understanding of the oceanic processes at the Antarctic Slope Front in the EWS, with possible implications for other sectors of Antarctica.

1. Introduction

A belt of floating ice shelves fringes the coastline of the Eastern Weddell Sea (EWS), draining a substantial fraction of the East Antarctic Ice Sheet into the Southern Ocean [*Melvold et al.*, 1998]. In this region, where glacial features cover large parts of the continental shelf, the amount of ice shelf basal melting is directly related to the oceanic processes over the continental slope. Previously, most attention has been given to the role of Warm Deep Water (WDW), which is the largest potential source of heat for basal melting in this sector of Antarctica [*Nicholls et al.*, 2009]. WDW normally resides below the shelf break depth north of the ice shelf front. But egresses of WDW onto the shelf and into the ice shelf cavities could lead to strong basal mass loss along the coast of the Weddell Sea [*Hellmer*, 2004; *Smedsrud et al.*, 2006], given its temperatures of about $+0.9^\circ$C. However, recent observations beneath the Fimbul Ice Shelf (FIS) at the Greenwich Meridian have shown that the access of WDW into the ice cavities is substantially more constrained than predicted by earlier modeling studies [*Hattermann et al.*, 2012]. Instead, the sub-ice shelf observations suggest that fresh, solar heated Antarctic Surface Water (ASW) plays an important role in providing the heat supply for basal melting. Subduction of this buoyant ASW below several hundred meters of ice is however a curious finding that raises questions regarding the driving mechanisms responsible for the spreading of fresh surface water throughout the water column.

In this study, we propose that ASW enters the ice shelf cavity after being brought on-shore by wind-driven surface Ekman transport and subsequent downwelling near the ice shelf front. Our working hypothesis is based on three facts: (1) stable easterly winds dominate the meteorology of the EWS coastal zone, leading to on-shore Ekman transport of surface water; (2) fresh and warm ASW down to a depth of roughly 200 m is a permanent feature along the ESW coast during summer and fall [*Sverdrup*, 1953; *Ohshima et al.*, 1996; *Heywood et al.*, 1998; *Nunez-Riboni and Fahrbach*, 2009; *Graham et al.*, 2013]; and (3) the ice shelf base depth is 150–200 m throughout this region [*Nøst*, 2004; *Timmermann et al.*, 2010], which is similar to the observed depth of ASW near the coast. In addition to our hypothesis, regarding the freshening of the coastal water column due to on-shore Ekman transport [*Sverdrup*, 1953; *Ohshima et al.*, 1996; *Nøst et al.*, 2011], *Fahrbach et al.* [1994] proposed that coastal waters may be substantially freshened by mixing with glacial meltwater,

© 2014. American Geophysical Union. All Rights Reserved.

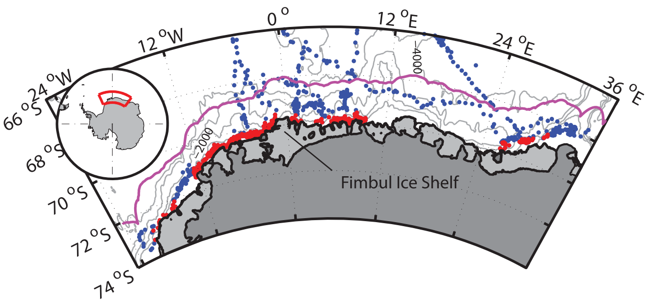

Figure 1. Map of the Eastern Weddell Sea. Light gray shading illustrates ice shelves and the magenta line indicates a distance of 100 km to the ice shelf front. Points denote locations where CTD profiles were collected by instrumented seals during February, March, and April. Profiles within 20 km from the ice shelf front are highlighted in red.

a mechanism that would imply substantial melting of ice shelves along the EWS coast. *Graham et al*. [2013] suggested the occurrence of local fresh water anomalies being advected along the coast.

We show that on-shore Ekman transport and downwelling in combination explain the observed accumulation of ASW near the ice shelf front and its subsequent spreading beneath the ice shelves, based on observations, scaling arguments, and numerical simulations. In section 2, we provide background information about water masses and coastal current features in the EWS. In section 3, we examine spatial and temporal variations in the coastal salinity field, using hydrography obtained by instrumented seals. In section 4, we derive an analytical model of the upper ocean momentum balance. In section 5, we use both idealized and regional general circulation ocean models to validate our hypothesis, and to investigate the fate of ASW in the ice cavity. We discuss results in section 6 and summarize our conclusions in section 7.

2. Background

2.1. Water Masses in the EWS

First, we briefly review the large-scale features of characteristic water masses in the region of interest. Our study area is the coastal zone of the EWS south of 66°S, extending roughly from 25°W to 36°E (Figure 1). This area covers the eastern and southern limits of the Weddell Gyre, which transports warm Circumpolar Deep Water from the central Southern Ocean southward, converting it into the slightly cooler and fresher WDW by the time it reaches the coast [*Nicholls et al*., 2009]. During austral winter, WDW in the deep ocean north of the Antarctic continental shelf is overlayed by a mixed layer of Winter Water (WW), which has a temperature near the surface freezing point and a salinity around 34.4 psu [*Nicholls et al*., 2009]. During summer, ASW is formed when the upper layer of WW is freshened by sea ice melting and warmed by the sun.

WDW is separated from the EWS coast by the Antarctic Slope Front (ASF) [*Heywood et al*., 1998]. The ASF is characterized by southward deepening isopycnals from about 100 m in the open ocean to more than 600 m at the continental slope [*Cisewski et al*., 2011]. The narrow continental shelves south of the ASF are occupied by low-salinity Eastern Shelf Water, which is a mixture of surface water (WW and ASW), glacial meltwater, and the modified WDW advected onto the shelf [*Fahrbach et al*., 1994]. The salinity of the Eastern Shelf Water exhibits strong seasonal variability, with a salinity below 34 psu during summer and a maximum value of 34.4 psu during later winter and spring (close to the WW salinity value) [*Nøst et al*., 2011]. In order to emphasize the seasonal extremes of the Eastern Shelf Water, we will use the terms ASW and WW to describe the water masses near the ice shelf front.

2.2. Coastal Current Features

Prevailing easterly winds along the coast induce on-shore transport in the surface Ekman layer. The convergence of surface water at the ice shelf front lifts the sea surface and induces a local regime of coastal downwelling. The accumulation of lighter surface water over the continental shelf, and its suppression due to coastal downwelling, induces the sloping isopycnals of the ASF. The density contrast across the front leads to a strong baroclinic current along the coast [*Heywood et al*., 1998; *Nunez-Riboni and Fahrbach*, 2009]. *Nøst et al*. [2011] found that the deepening of isopycnals caused by the wind-driven Ekman overturning is balanced by an eddy-driven overturning that acts to reduce the horizontal density gradient.

Here we propose that the downwelling process associated with the Ekman overturning is also the main mechanism responsible for the observed spreading of ASW through the coastal water column. Our analyses

© 2014. American Geophysical Union. All Rights Reserved.

show that the maximum downwelling depth of ASW is directly related to the balance between the wind-driven overturning and the counteracting eddy overturning. Furthermore, we hypothesize that with sufficiently strong downwelling, ASW can enter the ice shelf cavity, once it reaches the depth of the ice shelf front base.

3. Observations

In this section, we analyze observations of the coastal hydrography to explore the feasibility of on-shore Ekman transport and subsequent downwelling being the agent causing the accumulation of relatively fresh water masses along the EWS coast.

3.1. Data

Our data set is composed of conductivity-temperature-depth (CTD) profiles collected in the EWS from February to November 2008 by seven southern elephant seals instrumented with CTD-Satellite Relay Data Loggers, during the International Polar Year MEOP project (Marine Mammals Exploring the Oceans Pole to Pole). The instruments were glued to the fur on the heads of the seals, see *Biuw et al*. [2007] for details. The loggers reported vertical profiles of salinity, temperature, and pressure to depths of up to 2000 m. Each profile contains 17 depth points with corresponding temperature and salinity values. The first point in a dive occurs at a preselected depth (7 m in our study). Another dive point marks the deepest depth reached in a dive. Eight additional points are spread at preset intervals based on the maximum depth of the individual dive. The last seven points are selected between these other values by the so-called broken stick method [*Fedak et al*., 2002]. About 70% of the profiles have maximum depths less than 500 m, providing a unique tool for investigating the upper ocean processes along this sector of Antarctica. Accuracies are estimated to be better than 0.03 psu for salinity and 0.02°C for temperature. For a detailed description of data calibration see *Nøst et al*. [2011]. We will refer to the data set as "seal data" below. Because this study focuses on ASW that appears in summer and fall, we analyze all salinity profiles that were obtained during February, March, and April. This subset contains 1524 profiles taken at the locations indicated in Figure 1, with 1048 of them being within a distance of 20 km to the ice shelf front. We linearly interpolate each salinity profile onto a vertical grid of 1 m spacing from the 17 salinity observations before detailed analysis.

3.1.1. Observed Antarctic Surface Water distribution

First, we will investigate ASW distribution by examining the salinity field within 100 km of the ice shelf front. *Nøst et al*. [2011] found a rather uniform distribution of salinities in an along-shore direction. Their data show a gradual increase of salinity in time that appears to occur simultaneously in the far east and far west of their study region that extends more than 2000 km along the coast (see also Figure 5 therein). This suggests that the along-shore averaged salinity field is a reasonable first-order approximation of the hydrography along the EWS coast, and we proceed by analyzing the temporal evolution of the salinity distribution in a cross-shore direction.

Figure 2 presents the meridional cross-sections of salinity within 100 km of the ice shelf front for February, March, and April, respectively. The imagines are constructed by zonally averaging the vertically interpolated salinity profiles onto a horizontal grid with 5 km spacing in the cross-shore direction. In the figure, the boundary between the ASW and the WW layers is indicated by the 34 psu isohaline (the magenta lines); this definition is applied throughout the paper to emphasize the summer freshening in the upper ocean, even though the characteristic salinity of the WW is actually 34.4 psu. Figure 2 illustrates a systematic deepening of ASW from February through April. In February, a thin ASW layer extends over nearly the entire cross-section. In March, this layer has deepened to more than 200 m close to the ice shelf front and it has disappeared beyond 45 km from the ice shelf front. In April (Figure 2c), the ASW layer occupies about the same area as in March (Figure 2b), but it has higher salinities. This situation is likely explained by the onset of ice freezing at the surface and gradual mixing of ASW with the underlying WW.

Figure 3 shows a continuous time series of the along-slope-averaged salinity near the ice shelf front from February to April. The time series consists of all profiles within 10 km from the ice shelf front and has been smoothened with a 7 day running mean filter. The figure shows a gradual deepening of the ASW layer after February, reaching a maximum depth of more than 250 m toward the end of March, suggesting that the ASW layer continuously deepens near the ice shelf front during the summer.

© 2014. American Geophysical Union. All Rights Reserved.

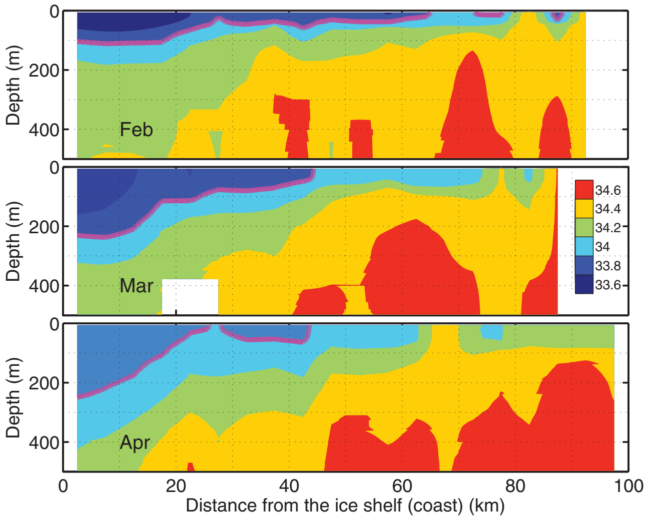

Figure 2. Zonal mean salinity against distance from the ice shelf front in (top) February, (middle) March, and (bottom) April. The thick magenta lines indicate the 34 psu isohaline.

Figures 2 and 3 also indicate that ASW near the ice shelf front during March and April reaches depths similar to or deeper than the ice shelf draft, which is about 200 m along the EWS coast [*Nøst*, 2004; *Timmermann et al*., 2010]. Figure 4 presents a map of ice shelf draft depth together with the locations of profiles collected by the seals which document ASW deeper than 200 m. The figure shows that the deepening of the ASW layer below the ice shelf front is a widespread phenomenon along the EWS coast. This implies that the ice shelf front draft is immersed in ASW and it is possible for ASW to spread beneath the ice shelf, as observed at the FIS by *Hattermann et al*. [2012].

3.2. Possible Explanations for the ASW Layer Deepening

The situation illustrated by Figure 2 is consistent with our hypothesis that on-shore Ekman transport leads to an accumulation of ASW near the ice shelf front during late summer and fall. However, the observed freshening of the coastal water column may also be caused by local melting of sea ice or ice shelves and in this subsection we discriminate between these different mechanisms.

To examine whether local sea ice melting is responsible for the deepening of the ASW layer near the ice shelf front, we compare the fresh water content estimated from the seal data with the fresh water input estimated from the sea ice thickness distribution. The fresh water content (FWC) indicates the amount of pure fresh water that is needed to freshen the water column relative to a reference water mass [*McPhee et al*., 2009], which can be calculated as

$$FWC = \int_{z_{lim}}^{0} \frac{S_{ref} - S(z)}{S_{ref}} dz. \quad (1)$$

Here $S(z)$ is the in situ salinity, and z_{lim} is the uppermost level where S equals the reference water mass salinity S_{ref}. For our analyses, we set S_{ref} to 34.4 psu and assume that variations in salinity due to surface freshening are small below the depth of z_{lim}. Figure 5a presents the fresh water content estimated from the salinity profiles from the seal data. The image is constructed by binning the results from individual profiles onto a regular grid of 1° longitude × 0.1° latitude. To estimate the uncertainties for the binned fresh water content shown in Figure 5a is challenging. First of all, calculating the fresh water content from the interpolated salinity profiles introduces uncertainties because of the limited vertical resolution of the seal data. Second, the number of observations varies from 1 to more than 100 in each bin,

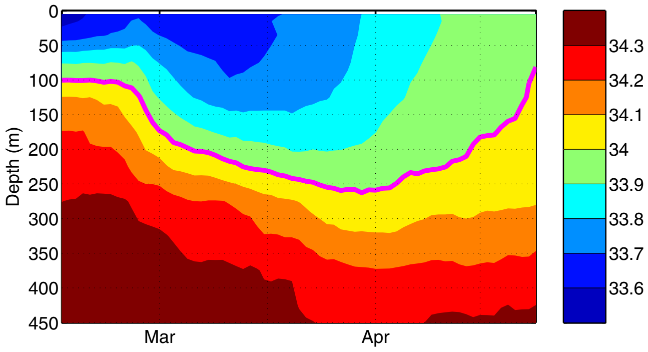

Figure 3. Time series of mean salinity within 10 km from the ice shelf front (coast). The thick magenta line indicates the 34 psu isohaline depth.

© 2014. American Geophysical Union. All Rights Reserved.

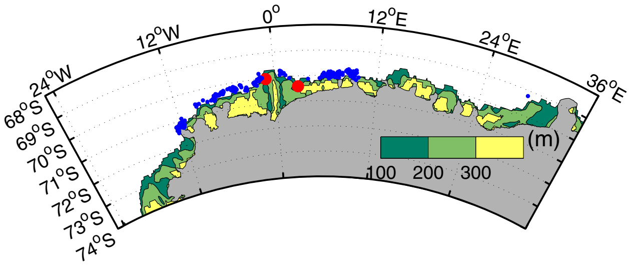

Figure 4. Ice shelf draft along the EWS coast (in m) [*Timmermann et al.*, 2010]. Blue dots indicate locations of CTD profiles which document ASW deeper than 200 m. Red dots indicate two mooring sites beneath the FIS where ASW has been observed [*Hattermann et al.*, 2012].

causing a lot of variability in the confidence intervals for the fresh water content at different locations. About half of the bins contain less than three profiles, which is not sufficient for a statistical error analysis. However, most of the bins near the ice shelf front consist of 10 profiles or more, and the average standard deviation of the fresh water content in these bins is 0.74 m.

The fresh water input (FWI) from local sea ice melting is related to sea ice thickness H_i, as

$$FWI=\frac{S_{ref}-S_i}{S_{ref}}H_i, \tag{2}$$

where S_i is the sea ice salinity. Sea ice salinity was observed to range from 4 to 10 psu during winter [*Eicken*, 1992] and here we set S_i to a constant value of 7 psu in equation (2). H_i values are from ship-based sea ice thickness measurements during the period 1982–2005, provided by the Antarctic Sea Ice Processes and Climate Program. A full description of data quality control and processing can be found in *Worby et al*. [2008]. ASW starts forming when sea ice melts in summer, so that the maximum sea ice thickness during later winter and early spring (October to December) likely represents the amount of fresh water that may be added locally to the water column, when neglecting the effect of sea ice drift. Therefore, we only use the ice thickness measurements collected within this period.

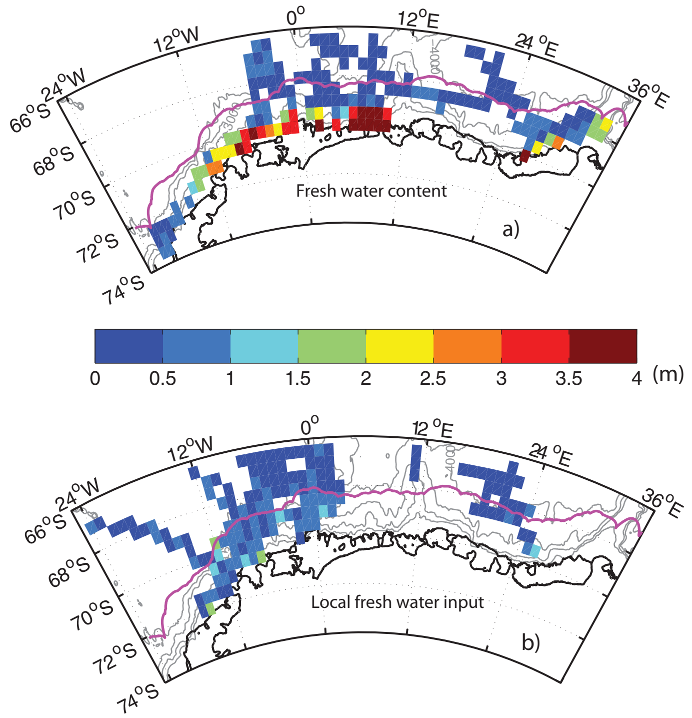

Figure 5. (a) The fresh water content estimated from the seal data, (b) the local fresh water input estimated from sea ice thickness [*Worby et al.*, 2008]. The magenta lines indicate a distance of 100 km to the ice shelf front.

Figure 5b presents the local fresh water input converted from the sea ice thickness measurements. The image is constructed by binning the fresh water input from individual sea ice measurements onto the same grid as in Figure 5a. Only five bins contain more than nine observations. Comparing Figure 5a with Figure 5b shows that the fresh water content and the local fresh water input from sea ice are roughly the same (0.5–1 m) away from the coast. Near the ice shelf front in contrast, the fresh water content generally exceeds the local fresh water input. Along most of the coast, the fresh water content is larger than 2 m, with a maximum value of more than 4 m, while the local fresh water input from sea ice is about 1 m at most places. We note that no sea ice thickness measurements are available near the coast on the east side of the FIS, where the seal data indicate a fresh water content of

© 2014. American Geophysical Union. All Rights Reserved.

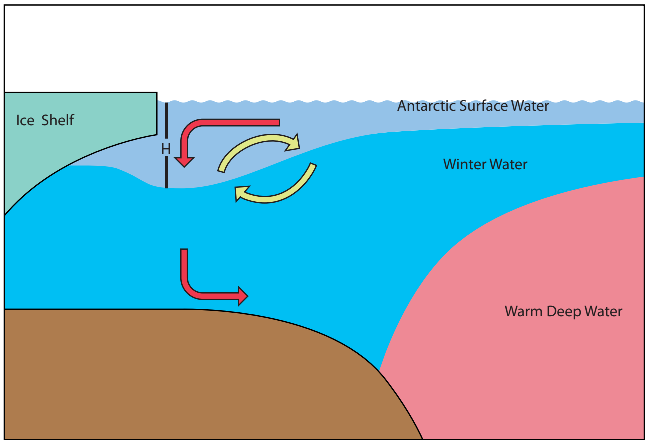

Figure 6. Sketch of a conceptual model of cross-shore circulation near the ice shelf front during summer. The red arrows indicate Ekman overturning and the yellow arrows indicate eddy overturning. Within the Antarctic Surface Water layer, on-shore Ekman transport is balanced by offshore eddy transport.

about 4 m. Multiyear measurements of seasonal fast ice in the unloading bay for the Norwegian overwintering station at roughly 5°E show a typical thickness of about 2–2.5 m, which is not sufficient to produce the observed amount of fresh water.

Figure 5a is based on salinity profiles collected during 2008 while Figure 5b shows sea ice measurements from the period between 1982 and 2005. Satellite passive-microwave data from 1979 to 2010 show that the Weddell Sea ice extent of 2007–2008 was not unusual compared to previous years. The mean sea ice thickness in the EWS between 1982 and 2005 is 0.73 m with a standard deviation of 0.77 m, and it is reasonable to assume that the sea ice thickness in 2007–2008 ranged about ±1 m plus that shown in Figure 5b. Also with this uncertainty taken into account, the local fresh water input in most places along the coast is smaller than the observed fresh water content, and we conclude that local sea ice melting may unlikely cause the observed freshening along the ice shelf front.

To investigate if basal melting can explain the observed freshening, we examine the changes in the fresh water content from February to March revealed by Figure 2. We estimate the integrated fresh water content in each month from the binned, zonally averaged, salinity field according to equation (1), using a reference salinity of 34.4 psu and integrating the fresh water content within 45 km of the ice shelf front. The length scale of 45 km is chosen because most of ASW is concentrated within this distance of the ice shelf front in March (Figure 2). The integrated fresh water contents are 0.87×10^5 m^2 and 1.28×10^5 m^2 in February and March, respectively, giving an increase of the integrated fresh water content of 0.41×10^5 m^2 within 1 month.

If the fresh water input is caused by basal melting, the average basal melt rate (BMR) can be deduced from the increase in the integrated fresh water content ($\Delta IFWC$) from February to March, using the following expression:

$$\Delta IFWC \times 12 = BMR \times D, \tag{3}$$

where D is the horizontal scale of the ice shelf in a cross-shore direction, which is about 100 km in the EWS. Setting $\Delta IFWC$ to 0.41×10^5 m^2 leads to an average basal melt rate BMR of 4.92 m per year, which is about 10 times larger than recent melting estimates from remote sensing [*Rignot et al*., 2013] and regional ocean modeling (T. Hattermann et al., Eddy-resolving model reveals two states of basal melting below Fimbul Ice Shelf, Antarctica, manuscript in revision at *Ocean Modelling*, 2014) for this region. Therefore, basal melting is unlikely to be the main reason for the deepening of the ASW layer near the ice shelf front.

Can on-shore Ekman transport of surface water near the ice front explain the observed freshening along the coast between February and March seen in Figure 2? Assuming a constant ASW salinity S_{ASW} in a two-layer system, equation (1) can be used to convert the change in the integrated fresh water content $\Delta IFWC$ into a change in the integrated ASW content within the coastal water column, as

$$\Delta IASW = \frac{S_{ref}}{S_{ref} - S_{ASW}} \Delta IFWC. \tag{4}$$

Setting $S_{ASW} = 33.7$ psu, which is a reasonable value for the average salinity of ASW being transported on-shore by winds, and inserting above mentioned values for the other parameters in equation (4) gives the

© 2014. American Geophysical Union. All Rights Reserved.

change in the integrated ASW content $\Delta IASW = 2.01 \times 10^6$ m^2. On the other hand, the Ekman transport of surface water over the period of 1 month can be estimated by multiplying the Ekman transport $\left(V = -\frac{\tau_s}{\rho_0 f}\right)$ with time (T = 30 days). Based on the analyses of near surface winds observed at an automatic weather station on the FIS (Hattermann et al., manuscript in revision, 2014), and wind fields from the Antarctic Ice Sheet Regional Atmospheric Climate Model [*Lenaerts et al*., 2012], we find a mean value for the easterly wind stress during 2010–2012 of roughly 0.1 N m^{-2}, with a minimum values close to zero and a maximum value of more than 0.2 N m^{-2}. Setting the wind stress τ_s to -0.1 N m^{-2}, the Coriolis parameter f to -1.35×10^{-4} s^{-1} and the reference density ρ_0 to 1027 kg m^{-3}, provides a on-shore transport of 1.87×10^6 m^2. This estimate is in the same range as the increase of the integrated ASW content deduced from the increase of the integrated fresh water content, suggesting that the accumulation of ASW near the ice shelf front may indeed be caused by wind-driven surface circulation.

4. Analytical Model

In order to explore our hypothesis that wind-driven downwelling is capable of depressing the surface water down to a depth at which it can access the ice shelf cavity, we derive an analytical expression for the downwelling depth of ASW based on an idealized model of the upper ocean momentum balance. The geometric configuration of this zonally averaged, two-layer dynamical model of the ASW and WW system is shown in Figure 6. At the very beginning of the ice-free season, ASW is formed within a thin surface layer, due to mixing of sea ice meltwater with the underlying WW. We assume that constant easterly wind drives ASW shoreward, such that the convergence of surface water near the ice shelf front deepens the interface between the two water masses near the coast. We propose that the ASW layer approaches its maximum depth when the system reaches a steady state, where the energy supply by wind is entirely balanced by dissipation due to eddies. The eddies are generated by the instability of the thermal wind flow that balances the density gradient across the sloping layer interface.

Similar ideas on the role of eddies for building an equilibrium in a system of wind-driven buoyant surface water have been investigated and applied to the Antarctic Circumpolar Current by *Marshall et al*. [2001] and *Karsten et al*. [2002], based on laboratory experiments and numerical simulations. In their dynamical framework, a first-order balance between Ekman overturning and eddy overturning is reached, which allows us to derive an expression for the downwelling depth. Here we focus on the balance between the eddy flux of mass and Ekman transport within the ASW layer. Suppose that the ASW layer has a thickness h and a cross-shore velocity v, and both can be decomposed into an Eulerian time-mean component and a fluctuating eddy component. Accordingly, the net transport within this layer hv can be written as

$$\overline{hv} = \overline{(\bar{h}+h')(\bar{v}+v')} = \bar{h}\bar{v} + \overline{h'v'}. \tag{5}$$

Here overbars denote the temporal average and primes indicate temporal deviations, which represent contributions due to the eddies. We assume that the Eulerian mean transport in a cross-shore direction within the ASW layer is set by the Ekman transport

$$\bar{h}\bar{v} = -\frac{\tau_s}{\rho_0 f}. \tag{6}$$

In the first order, this on-shore surface transport is fully balanced by counteracting eddy fluxes at the layer interface, such that the total cross-shore time-mean transport $\overline{hv}$ disappears. Inserting equation (6) into equation (5) thus yields the following expression for the upper ocean momentum balance

$$\frac{\tau_s}{\rho_0 f} = \overline{h'v'}. \tag{7}$$

In their eddy closure parameterization, *Gent and McWilliams* [1990] proposed that fluxes within an isopycnal layer are directly proportional to the mean gradient of layer thickness, relating the eddy transport on the right-hand side of equation (7) directly to the slope of the interface between ASW and the WW

©2014. American Geophysical Union. All Rights Reserved.

$$\overline{h'v'} = -K\frac{\partial h}{\partial y}, \tag{8}$$

where K is defined as the eddy diffusivity for layer thickness, also referred to the thickness diffusivity. However, to determine the value of K is one of the largest challenges facing the oceanographic community. While the simplest approach would be assuming a constant K, a number of studies have suggested that K is itself a function of the slope of the interface [*Visbeck et al*., 1997; *Marshall and Radko*, 2003], i.e.,

$$K = -k\frac{\partial h}{\partial y}, \tag{9}$$

where k is a constant of proportionality which is found to be in the order of 10^6 m^2 s^{-1} for the Antarctic Circumpolar Current regime [*Marshall and Radko*, 2003]. Combining equations (7–9) gives

$$k\left(\frac{\partial h}{\partial y}\right)^2 = \frac{\tau_s}{f\rho_0}. \tag{10}$$

As illustrated in Figure 6, the layer thickness h near the ice shelf front can be interpreted as the maximum downwelling depth of ASW, indicated by "H" in Figure 6. Rearranging equation (10) yields the following scaling relation:

$$H \sim \left(\frac{L^2}{k|f|\rho_0}\right)^{1/2} |\tau_s|^{1/2}, \tag{11}$$

where L is a meridional dynamical scale of the system.

Note that equation (11) indicates a downwelling depth that depends on the square root of the surface wind stress. This solution is formally equivalent to the expression for thermocline depth derived by *Marshall and Radko* [2003] for the ACC in the case of a vanishing residual overturning circulation (equation (20) in their paper).

Along the EWS coast, the meridional dynamical scale L, on which the easterly wind has effects, is in the order of 100 km (also see the top and middle plots of Figure 2). In equation (11), setting L to 100 km and f, $\rho_{0,}$ and τ_s to the same values as we use in section 3.2 yields a scale of the downwelling depth in the order of 100 m, which is agreement with the observations (Figure 2). This supports our hypothesis that wind-driven downwelling is capable of depressing ASW similar to the depth of the ice shelf draft.

5. Numerical Modeling

In this section, we analyze a set of different numerical simulations of the coastal circulation to investigate the linear dependency of the downwelling depth on the surface wind stress, as well as to explore the role of downwelling in the access of ASW beneath the ice shelf.

5.1. Idealized Model of the Coastal Circulation

We simulate the circulation along the EWS coast in a simplified, periodic channel geometry, using an ice shelf-augmented version [*Dinniman et al*., 2009; *Galton-Fenzi et al*., 2012] of the Regional Ocean Modelling System (ROMS) [*Shchepetkin and McWilliams*, 2005]. A similar version of this model was employed by *Nøst et al*. [2011] to study the role of eddies for transporting WDW toward the ice shelf cavities. The slightly modified model domain in our study consists of a 480 km long and 300 km wide channel. The model topography varies in a cross-channel direction with an ice shelf cavity (750 m depth) in the south that connects to the deep ocean (2000 m depth) via a 400 m deep sill (Figure 7a). In order to highlight the role of the downwelling depth for the spreading of ASW into the ice shelf cavity, the ice shelf is of uniform thickness (150 m) extending from the southern boundary toward the continental slope. For computational efficiency, the horizontal resolution is reduced from 1.5 km in *Nøst et al*. [2011] to 2 km, with minor effects on the representation of eddy fluxes across the front. Other technical aspects of the model, which consists of

©2014. American Geophysical Union. All Rights Reserved.

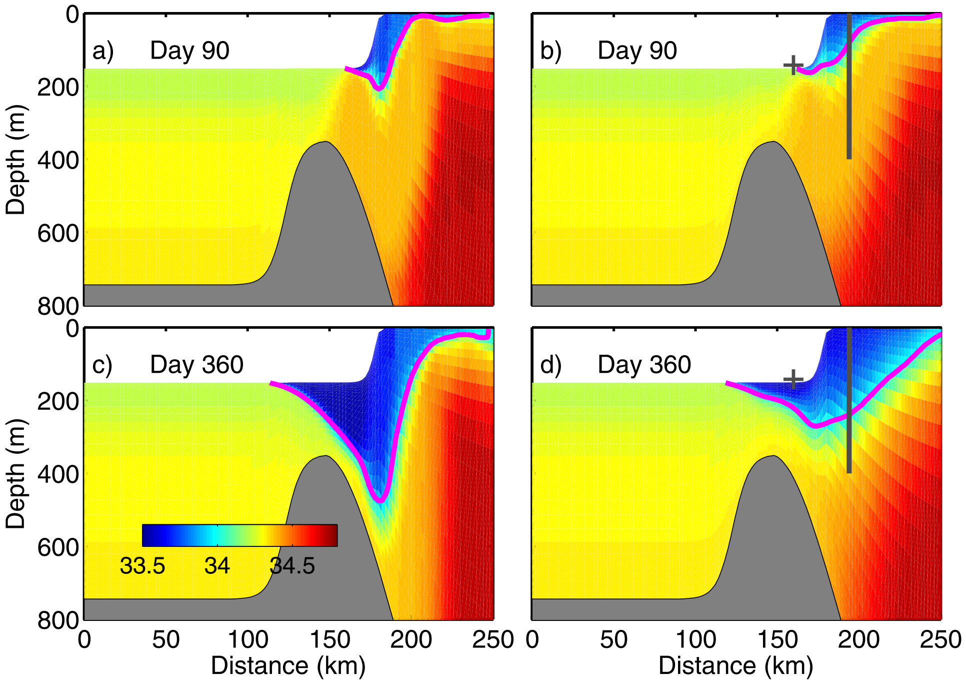

Figure 7. (a,c) and (b,d) are along-slope-averaged salinity fields from daily snapshots from the $2D_9$ experiment and the REL_9 experiment, respectively. The thick magenta lines indicate the 34 psu isohalines. The gray crosses in Figures 7b and 7d indicate a location in the ice cavity 20 km south of the ice shelf front. The thick gray lines in Figures 7b and 7d indicate a location in the open ocean 10 km north of the ice shelf front.

30 terrain-following vertical layers implemented on an f-plane, are identical to the model presented by *Nøst et al.* [2011].

With this idealized model setup, two different sets of experiments are conducted, referred to as "relaxation experiments" and "annual experiments", respectively. The relaxation experiments study how the transient adjustment between the Ekman overturning and the eddy overturning affects the ASW transport under different wind forcings. The annual experiments investigate further the time scale and efficiency of the seasonal downwelling in a quasi-steady annual-cycle scenario. Both the relaxation experiments and the annual experiments are forced with different horizontally uniform, constant in time, easterly wind stress fields: a weak wind forcing of 3 m s^{-1}(0.02 N m^{-2} in wind stress); a moderate wind forcings of 6 and 9 m s^{-1} (0.07 and 0.15 N m^{-2} in wind stress); and a strong wind forcing of 12 m s^{-1} (0.26 N m^{-2} in wind stress). An additional relaxation experiment is conducted to examine the role of eddies in building coastal momentum balance. This experiment is identical to the relaxation experiment with 9 m s^{-1} wind forcing, except that it only uses four along-shore grid points to mimic a two-dimensional setup, in which eddies cannot evolve. In total, there are nine idealized experiments which are summarized in Table 1. The three-dimensional relaxation experiments and the annual experiments are denoted with "REL_*" and "ANN_*," respectively, with an underscore denoting the strength of the wind forcing. The two-dimensional relaxation experiment is referred to as "$2D_9$."

Table 1. Idealized Model Experiments, With the Letters Corresponding to Particular Model Setups and the Numbers to Wind Forcings

	Wind			
	3 m/s	6 m/s	9 m/s	12 m/s
Additional experiment		$2D_9$		
Relaxation experiments	REL_3	REL_6	REL_9	REL_{12}
Annual experiments	ANN_3	ANN_6	ANN_9	ANN_{12}

© 2014. American Geophysical Union. All Rights Reserved.

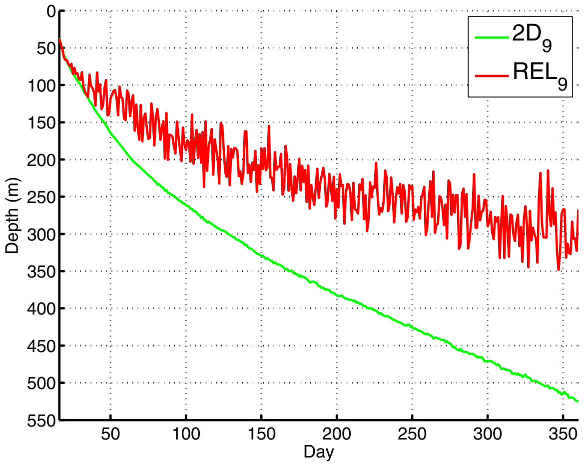

Figure 8. Time series of daily maximum depth of the 34 psu isohaline along the central section of the $2D_9$ and REL_9 experiments.

5.1.1. Relaxation Experiments

The relaxation experiments are initialized in the same way as described by *Nøst et al.* [2011], with a typical winter situation, in which only WW is present near the coast. ASW is gradually introduced at the ocean surface, by relaxing the surface temperature to −1.75°C and salinity to 33.7 psu, with a nudging time scale of 3 days. Water masses in the model interior are circulated freely via the counteracting Ekman and eddy overturning circulations that adjust freely during the model integration. All of the relaxation experiments are integrated for one model year (360 days).

Before exploring the relationship between wind stress and downwelling depth in detail, we first assess the role of mesoscale eddies in building a cross-shore momentum balance in the upper ocean, by comparing model results from the $2D_9$ experiment with the REL_9 experiment. Figure 7 shows the zonally averaged salinity fields from daily snapshots in these two experiments for Day 90 and Day 360. Both experiments reproduce the accumulation and downwelling of ASW near the ice shelf front and its spreading into the ice shelf cavity. However, the downwelling of ASW near the ice shelf front in $2D_9$ generally reaches deeper than that in REL_9. In detail, the maximum depth of ASW at Day 90 in $2D_9$ is about 250 m (top left), while the maximum depth in REL_9 is about 170 m in this time frame (top right). At Day 360 (two bottom plots in Figure 7), the difference between the maximum depths of ASW becomes more significant, with a maximum depth of more than 500 m in $2D_9$ and a maximum depth of about 300 m in REL_9.

Figure 8 presents daily time series of the maximum ASW depth within 20 km of the ice shelf front along the central section of the model domain ($j=120$) for the $2D_9$ and REL_9 experiments. The figure shows that the downwelling depth in REL_9(red lines) increases with time, accompanied by eddy-like fluctuations. After an initial rapid deepening of ASW, subsequent to Day 30, eddies begin to form and the downwelling depth increases at a lower rate. After about Day 100, the downwelling depth starts to level off with sufficiently large eddy activities, reaching a quasi-equilibrium state. In contrast, the depth of ASW in $2D_9$ (green lines) increases throughout the experiment, with no equilibrium being reached during the simulation period. This leads to an unrealistically sharp, almost vertical front near the ice shelf in $2D_9$ (Figure 7c), demonstrating the importance of the eddy overturning for balancing the energy input due to winds and for leveling the isopycnals.

We now examine the effect of varying wind stress on the downwelling depth of ASW. Figure 9a presents temporal evolution of the maximum ASW depth near the ice shelf front for all four wind forcings (time series produced in the same way as in Figure 8). The figure shows that stronger winds generally lead to deeper downwelling. The analytical model presented in section 4 suggests that the downwelling depth is a linear function of the square root of the wind stress (equation (11)), with a slope of 300 s $m^{3/2}$ $kg^{-1/2}$ $((\frac{L^2}{kf\rho_0})^{1/2})$ based on the input values in that section. Figure 9b shows a plot of the downwelling depth against the square root of the wind stress at Day 150, taken from an 8 day moving average of the time series shown in Figure 9a. A linear regression of the downwelling depth (shown by the thick black line in Figure 9b) gives a slope of 560 s $m^{3/2}$ $kg^{-1/2}$ with a correlation coefficient of 0.99. The slope from other time points between Day 100 and Day 250 are in the same order of magnitude, indicating a robust relationship between the downwelling depth and the wind stress. The slope estimated from numerical simulations differs by almost a factor of two from the solution of the analytical model. However, given the simplicity of the models, the agreement within the same order of magnitude indicates that both models consistently capture the basic dynamics determining the downwelling depth along the coast.

Figure 9a also shows that ASW reaches the depth of the ice shelf front (150 m) after about 200 days in REL_6 and after 50 days in REL_{12}. In reality, ASW forms when sea ice starts melting in December [*Nicholls et al.*,

© 2014. American Geophysical Union. All Rights Reserved.

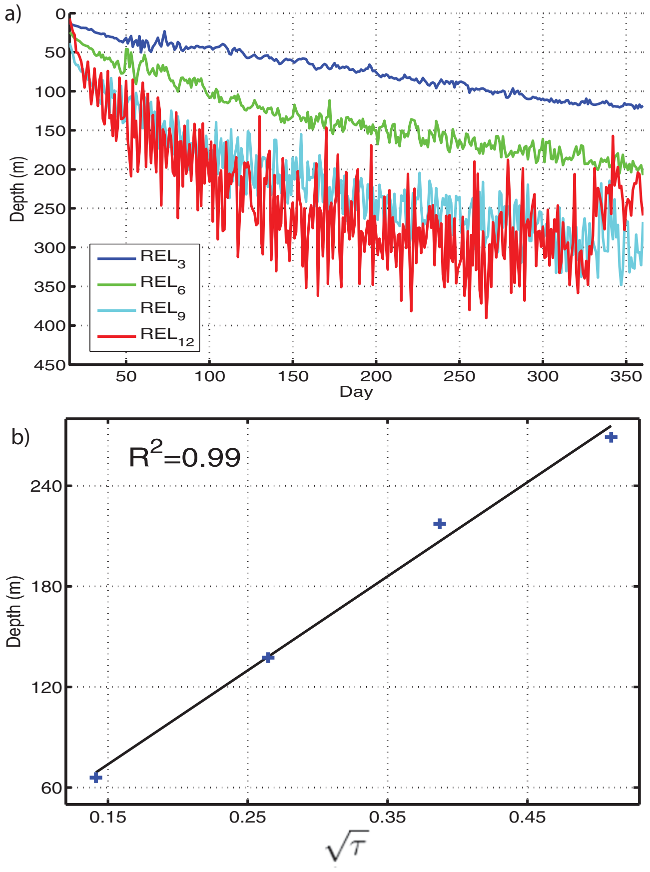

Figure 9. (a) Time series of daily maximum depth of the 34 psu isohaline along the central section of the model domain from all of the four relaxation experiments (four different wind forcings). (b) Downwelling depth against square root of the wind stresses at Day 150 for the relaxation experiments (blue crosses). The thick black line indicates the linear trend.

2009], and it usually appears down to a depth of more than 200 m 3–4 months later (Figure 2b). Therefore, the time scale at which the coastal downwelling suppresses ASW along the coast is an important criteria that will be examined using results from the annual experiments in the next subsection.

5.1.2. Annual Experiments

The annual experiments are essentially an extension of the relaxation runs with additional water mass restoration at the model boundaries to assure a quasi-steady annual cycle. To mimic the seasonal surface freshening by sea ice melting, the surface salinity and temperature are restored to horizontal uniform climatological values with a nudging time scale of 10 days. A time series of this climatological surface hydrography, which is obtained by spatial averaging and daily binning of the seal data as described by Hattermann et al. (manuscript in revision, 2014), is presented in Figure 10a. The seal data cover the period between February and October, while the data gap at the beginning and the end of the year were filled by linear interpolation, assuming an annual periodicity. In addition, a constant nudging at the eastern (inflow) model boundary is applied, to preserve frontal structure of the ASF over the continental slope. However, in order to allow the upper ocean properties to evolve freely as a response to the surface forcing, the nudging, which restores temperature and salinity toward the model's initial field, is only applied at depths below the ASF thermocline (the depth of the -0.3°C isotherm). The applied nudging time scale varies linearly from 3 days at the boundary grid point, to 10 days at the end of the 30 km wide nudging zone. Furthermore, temperature and salinity are restored to the initial conditions with a time scale of 30 days within a 10 km wide nudging zone along the northern channel wall, in order to compensate for upwelling effects due to the Ekman overturning circulation. Each annual experiment is started from a quasi-steady spin-up simulation and is integrated for five model years. The spin-up is initialized in the same way as the relaxation experiments presented in section 5.1.1 and run for 10 years with constant winter surface hydrography ($S = 34.3$ psu and $T = -1.9^{\circ}$C) and a constant easterly wind forcing of 9 m s^{-1}.

We first examine the upper ocean water masses along the coast from an annual experiment under moderate wind forcing (ANN_9). Figure 10b presents a time series of along-slope-averaged salinity profiles as well as along-slope-averaged depths of the 34 psu isohaline at a location 10 km north of the front. The upper ocean water masses experience a seasonal cycle, with ASW periodically appearing and disappearing from the water column. ASW first appears in February, and becomes continuously deeper, reaching a maximum depth of 170 m in July. After July, the ASW layer becomes shallower and gradually disappears from the water column in September. In addition, comparing the ASW layer depth with the ice draft depth in Figure 10b shows that the depressed ASW exceeds the ice draft periodically from May to August.

© 2014. American Geophysical Union. All Rights Reserved.

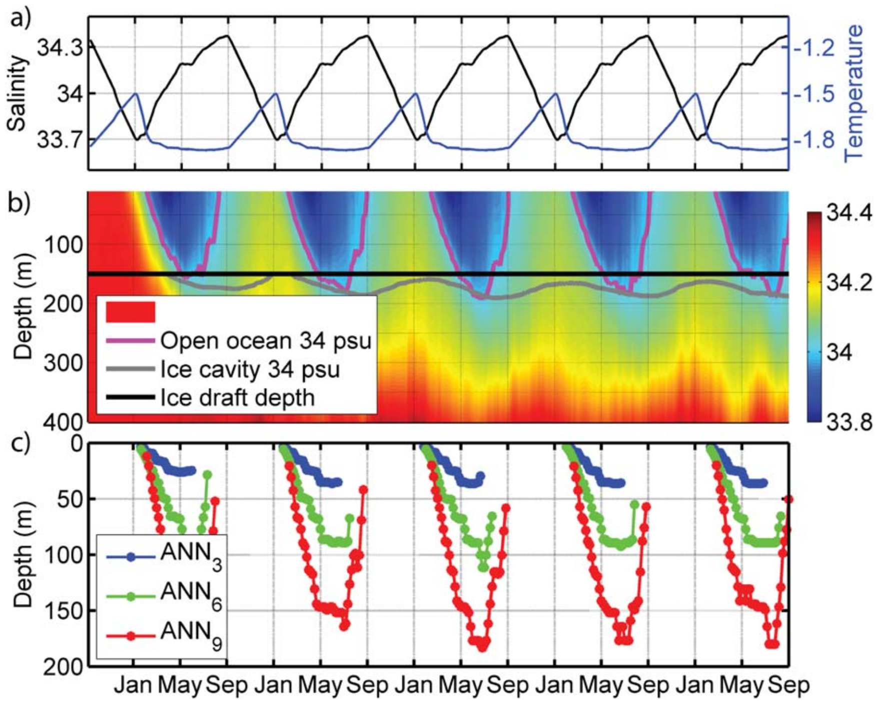

Figure 10. (a) Time series of surface salinities and temperatures toward which surface water in the seasonal experiments are restored, (b) time series of along-slope-averaged salinity profiles at a location 10 km north of the ice shelf front (indicated by the thick gray line in Figure 7b); the magenta lines indicate the 34 psu isohaline depth at this location. The gray line indicates along-slope-averaged depth of the 34 psu isohalines at a location 20 km south of the ice shelf front (i.e., in the ice cavity). The thick black line indicates the ice draft depth. (c) Time series of along-slope-averaged maximum depths of the 34 psu isohaline under different wind forcings.

Figure 10c shows time series of the along-slope-averaged maximum depth of the 34 psu isohaline within 20 km of the ice shelf front for the ANN_3, ANN_6, and ANN_9 experiments. The ANN_{12} experiment, which is omitted for clarity of the figure, shows similar average depths as the ANN_9 run, but with larger spatial and temporal variability due to stronger eddy activity. All experiments reproduce a seasonal periodicity, in which the timing of the maximum extent of ASW throughout the water column is largely independent of the wind forcing. Furthermore, the downwelling depth increases with stronger winds, and a linear regression of the respective maximum depth of different experiments to $\sqrt{\tau}$ yields a slope of 320 s $m^{3/2}$ $kg^{-1/2}$ ($R^2 = 0.84$), which is consistent with the results from the relaxation experiments.

Figure 10b also shows a time series of the along-slope-averaged depth of the 34 psu isohaline at a location 20 km south of the ice shelf front in the ice cavity. Comparing this time series with its counterpart in the open ocean (gray and magenta lines in Figure 10b) shows that the 34 psu isohaline reaches its maximum depth beneath the ice about 2 months later than in the open ocean. Further analysis shows that the upper ocean water mass within 60 km of the ice shelf front in the cavity are subject to an annual variability (not shown) that lags behind the open ocean seasonal cycle. This is consistent with the proposition that the fresh water successively propagates into the ice shelf cavity as a result of the wind-driven coastal downwelling.

5.2. Regional Modeling for the Fimbul Ice Shelf region

In this section, we investigate the fate of ASW inside the ice cavity by analyzing results from a high-resolution (1.5 km) regional model for the FIS region. This model was recently presented by Hattermann et al. (manuscript in revision, 2014) who conducted a set of different experiments to study basal melting at the FIS. They found that the presence of ASW is likely to affect basal melting at the FIS in several ways, with a net increase of the area-averaged melt rate by about 5 cm per year when ASW is included in the model. Here we analyze results from their experiment ANN-100, which employed the most realistic forcing and resembled the subice observations of [*Hattermann et al*., 2012]. The ANN-100 setup is similar to the idealized annual experiments presented in section 5.1.2, except that it uses realistic model geometry and surface

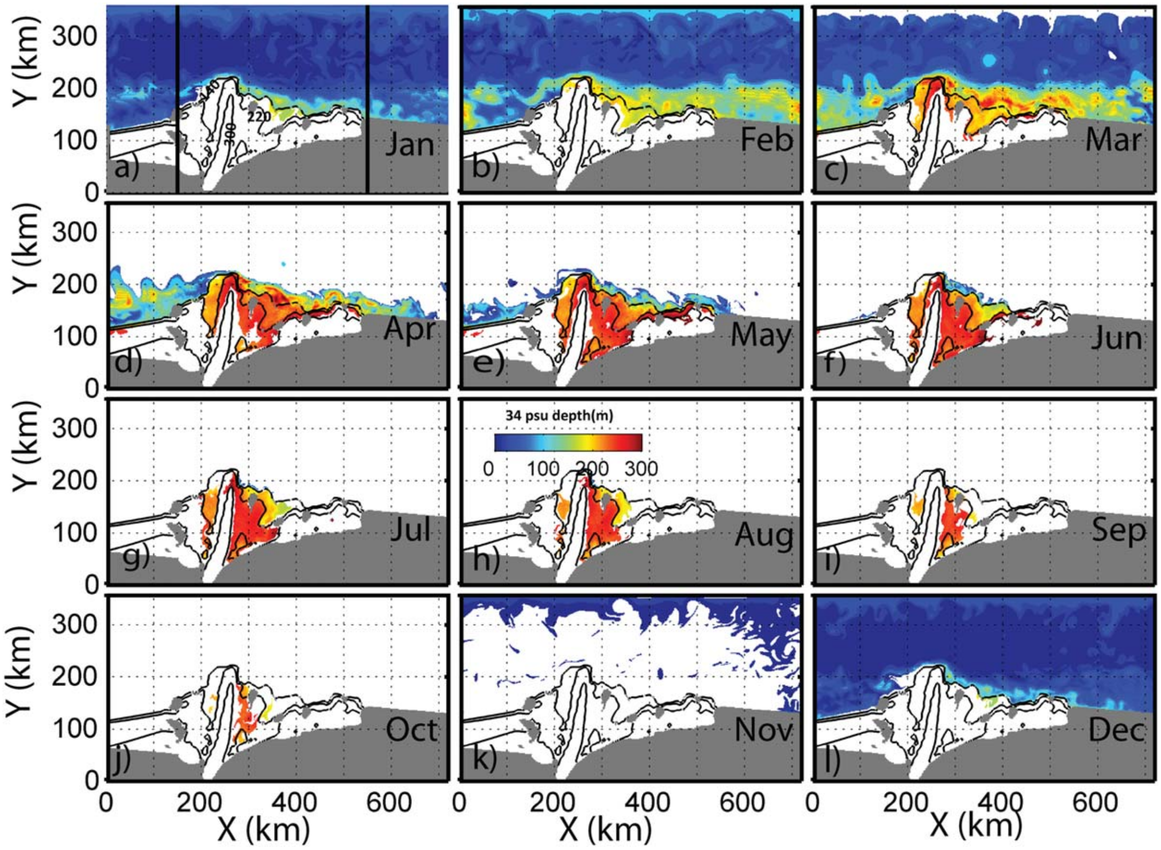

Figure 11. Snapshots of spatial distributions of the 34 psu isohaline depths on the first day of each month from the ANN-100 experiment. The black lines show the ice draft depth contours at 140, 220, and 300 m. The two thick black vertical lines in (a) indicate the central part of the east-west periodic channel which realistically represents the topography of the Fimbul Ice Shelf area.

wind forcing specific for the FIS region and also the hydrography above the thermocline at the eastern boundary is restored to climatological values. For a more detailed description of the ANN-100 experiment, as well as for the details of the model setup, the reader is referred to Hattermann et al. (manuscript in revision, 2014).

The ANN-100 simulation supports our hypothesis that surface water enters the FIS cavity after being accumulated near the ice shelf front due to on-shore Ekman transport. This can be seen in Figure 11, which illustrates the evolution of the ASW layer throughout the year, by showing the depth of the 34 psu isohaline within the model domain. In December, ASW is distributed over the entire model domain within a thin surface layer with a uniform thickness of about 50 m except for within a narrow belt close to the ice shelf front on the east side of the ice tongue, where the ASW layer is located at about 100 m (Figure 11l). During the following months, the on-shore surface Ekman transport leads to a successive deepening of the ASW layer near the ice shelf front, from about 150 m in January to more than 250 m in March, although surface conditions are restored uniformly over the entire model domain. ASW starts spreading beneath the ice shelf once the downwelling depth exceeds the ice draft depth, as indicated by the same color shading on either side of the 140 m ice draft lines in Figures 11a and 11b.

The spatial distribution of ASW beneath the ice shelf appears to be strongly affected by the ice shelf geometry. Figure 11 shows that ASW starts accumulating near the ice front earlier and extends deeper on the east side of the ice tongue in January, February, and March (see Figures 11a–11c). Consequently, ASW spreads into the ice shelf cavity earlier in the east than in the west, which is consistent with observations that have shown that ASW first appears in the ice cavity on the east side of the FIS [*Hattermann et al.*, 2012]. Once beneath the ice, the spreading of ASW appears to be guided by the ice base topography. Figures 11c–11l

© 2014. American Geophysical Union. All Rights Reserved.

shows that ASW reaches most of the ice base except the thick keel of ice in the central part of the FIS, confined by the 300 m ice draft contours. This supports our suggestion that the access of ASW is primarily determined by the maximum downwelling depth near the ice shelf front, which reaches about 300 m in April, as shown by the orange patches near the ice front in Figure 11d.

The model also shows that ASW is circulated far into the ice shelf cavity, and that it remains beneath the ice also throughout the winter season. This can be seen from the orange patches beneath the ice shelf between July and October (Figures 11f–11j), which show that the seasonal cycle of water mass exchange beneath the ice is several months delayed compared to seasonal variations at the surface in the open ocean. The time scale of the delay appears to be mainly determined by the time it takes for the wind-driven downwelling to suppress the surface water to a depth from which it can access the ice base.

6. Discussion

Based on the large number of salinity profiles collected by instrumented seals in the MEOP programme, we revisit the seasonal deepening of the ASW layer during late summer and fall near the ice shelf front in the EWS. While the coastal current is likely to propagate localized freshening signals along the coast [*Graham et al*., 2013], along-slope advection alone cannot explain the simultaneous deepening of the ASW layer, which is observed over a distance of more than 2000 km along the EWS coast [*Nøst et al*., 2011]. Also local melting of sea ice or ice shelves is not capable to provide sufficient fresh water input to cause the observed freshening of substantial parts of the coastal water column. Instead, our analyses of the coastal salinity field confirm the hypothesis that on-shore Ekman transport is the main mechanism responsible for the accumulation of ASW near the ice shelf front [*Sverdrup*, 1953; *Ohshima et al*., 1996; *Nøst et al*., 2011].

The seal data show that the ASW layer reaches its maximum depth at the end of March and disappears from the water column by the end of May [*Nøst et al*., 2011] (Figure 6, therein). In comparison, the simulated seasonal cycle in our annual experiment in the current study lags behind the observations by several months, with a maximum downwelling depth in the model in July and ASW being present until September. This delay is likely an effect of the simplified hydrography used for the restoring conditions at the model surface, which may not fully capture the ice/ocean interaction during the sea ice freezing period. Nevertheless, both the ANN_6 and the ANN_9 experiments show an ASW layer depth that is comparable to the ice shelf depth already in April and May, confirming that wind-driven downwelling is capable to transport ASW beneath the ice shelf on seasonal time scales.

In reality, other effects such as tides and local topography further complicate the exchange between the open ocean and the ice shelf cavity [*Nicholls et al*., 2009]. In our idealized model setup, uncertainty is added, because the abrupt ice shelf edge needs to be replaced by a smoother transition to open water. This topographical smoothing, which is necessary to minimize the pressure gradient force error associated with S-coordinate models, reduces the potential vorticity barrier imposed by the ice front and likely increases the exchange at the ice shelf front. However, test runs with different frontal slopes show no qualitative differences in the spreading of ASW beneath the ice shelf. Instead, we find that ASW spreads beneath the ice shelf once the downwelling depth is deeper than the ice shelf draft.

Since the presence of ASW in the ice shelf cavity has effects both on basal melting, as well as subice circulation (Hattermann et al., manuscript in revision, 2014), it is important to know where ASW enters beneath the Antarctic ice shelves. Our study suggests that possible spreading sites can be identified by determining the downwelling depth based on the coastal wind field, in comparison with the depth of the ice shelf draft. As a first-order approximation, the downwelling depth depends directly on the along-shore wind stress component, suggesting that ice shelves might be more affected by solar heated surface water in a future climate where Antarctic coastal wind strength is likely to increase [*Kushner et al*., 2001]. But it is important to note that the downwelling depth does not respond linearly to the wind forcing, and becomes less sensitive for increasing wind stress. A similar nonlinear response of the eddy overturning to wind forcing has been proposed for the response of the Antarctic Circumpolar Current [*Hallberg and Gnanadesikan*, 2001, 2006; *Munday et al*., 2013], which is usually referred to as "eddy saturation." Here, we simply assume that the eddy diffusivity K is a linear function of the slope of the interface, which yields an expression for the downwelling depth (equation (11)) that is qualitatively confirmed by numerical experiments. However, a proper

© 2014. American Geophysical Union. All Rights Reserved.

investigation of nonlinear relationship between downwelling depth and wind stress should be the subject of future work.

Our study of surface processes over the EWS continental shelf complements the work of *Nøst et al*. [2011], which focused on exchanges in depth. *Nøst et al*. [2011] suggested that wind-driven Ekman overturning creates the ASF between the WW and WDW, feeding a deep ocean eddy overturning that causes upward-sloping isopycnals along the seabed and transports modified WDW onto the continental shelf. In agreement with Hattermann et al. (manuscript in revision, 2014), we find that this situation is further complicated by a shallower frontal system, introduced by the presence of buoyant surface water. To show this, we conducted an additional 3-D relaxation experiment, which is identical to the REL_9 experiment, except that no ASW is introduced at the surface. Results from this experiment show an on-shore transport of modified WDW and upward-sloping isopycnals, similar to the scenario described by *Nøst et al*. [2011]. In contrast, the upward-sloping isopycnals disappear when ASW is introduced at the ocean surface in the REL_9 experiment, indicating that the deep ocean heat transport is directly affected by the upper ocean stratification. Although the exact mechanism for this interaction remains unresolved, our results are consistent with Hattermann et al. (manuscript in revision, 2014), who reported that the eddy-driven inflow of modified WDW is more constrained when ASW is present near the ice shelf front in late summer and fall.

7. Conclusion

By combining observations, scaling arguments and numerical simulations, we investigate the mechanism for the appearance of Antarctic Surface Water in the Fimbul Ice Shelf cavity observed by [*Hattermann et al*., 2012]. We find that ASW enters the ice shelf cavity after being brought on-shore and accumulated along the ice shelf front in a regime of coastal downwelling. ASW spreads beneath the ice shelf when the downwelling reaches the depth of ice shelf base. Mesoscale eddies play an important role in building the coastal momentum balance and thus determine the downwelling depth, which can be approximated as a nonlinear function of the along shore wind stress. It is likely that the spreading of ASW beneath Antarctic ice shelves occurs where on-shore surface Ekman transport dominates cross-shore coastal circulation during summer. The relation between the downwelling depth and the wind stress developed in this study can be used as a tool to find such locations, by examining the wind field and the ice shelf draft.

Acknowledgments
This research was supported by the International Polar Year Project, MEOP (Marine Mammals Exploring the Oceans Pole to Pole) and by the NORKLIMA project 229764/E10, both are Norwegian Research Council Programmes.

References

Biuw, M., et al. (2007), Variations in behavior and condition of a southern ocean top predator in relation to in situ oceanographic conditions, *Proc. Natl. Acad. Sci. U. S. A.*, *104*, 13,705–13,710.

Cisewski, B., W. Strass, and H. Leach (2011), Circulation and transport of water masses in the Lazarev Sea, Antarctica, during summer and winter 2006, *Deep Sea Res., Part I*, *58*, 186–199.

Dinniman, M., J. M. Klinck, and W. O. Smith (2009), Influence of sea ice cover and icebergs on circulation and water mass formation in a numerical circulation model of the Ross Sea, Antarctica, *J. Geophys. Res.*, *112*, C11013, doi:10.1029/2006JC004036.

Eicken, H. (1992), Salinity profiles of Antarctic sea ice: Filed data and model results, *J. Geophys. Res.*, *97*, 15,545–15,557.

Fahrbach, E., R. G. Peterson, G. Rohardt, P. Schlosser, and R. Bayer (1994), Suppression of bottom water formation in the south-eastern Weddell Sea, *Deep Sea Res., Part I*, *41*, 389–411.

Fedak, M., P. Lovell, B. McConnell, and C. Hunter (2002), Overcoming the constraints of long range radio telemetry from animals: Getting more useful data from smaller packages, *Integr. Comp. Biol.*, *42*, 3–10.

Galton-Fenzi, B. K., J. Hunter, R. Coleman, S. J. Marsland, and R. C. Warner (2012), Modeling the basal melting and marine ice accretion of the Amery Ice Shelf, *J. Geophys. Res.*, *117*, C09031, doi:10.1029/2012JC008214.

Gent, P. R., and J. C. McWilliams (1990), Isopycnal mixing in ocean circulation models, *J. Phys. Oceanogr.*, *20*, 150–155.

Graham, J. A., K. J. Heywood, C. P. Chavanne, and P. R. Holland (2013), Seasonal variability of water masses and transport on the Antarctic continental shelf and slope in the southeast Weddell Sea, *J. Geophys. Res.*, *118*, 2201–2214, doi:10.1002/jgrc.20174.

Hallberg, R., and A. Gnanadesikan (2001), An exploration of the role of transient eddies in determining the transport of a zonally reentrant current, *J. Phys. Oceanogr.*, *31*, 3312–3310.

Hallberg, R., and A. Gnanadesikan (2006), The role of eddies in determining the structure and response of the wind-driven Southern Hemisphere overturning: Results from the modeling eddies in the Southern Ocean (MESO) project, *J. Phys. Oceanogr.*, *36*, 2232–2252.

Hattermann, T., O. Nøst, J. Lilly, and L. Smedsrud (2012), Two years of oceanic observations below the Fimbul Ice Shelf, *Geophys. Res. Lett.*, *39*, L12605, doi:10.1029/2012GL051012.

Hellmer, H. H. (2004), Impact of Antarctic ice shelf basal melting on sea ice and deep ocean properties, *Geophys. Res. Lett.*, *31*, L10307, doi: 10.1029/2004GL019506.

Heywood, K., R. Locarnini, R. Frew, P. Dennis, and B. King (1998), Transport and water masses of the Antarctic Slope Front System in the eastern Weddell Sea, in *Ocean, Ice and Atmosphere: Interactions at the Antarctic Continental Margin, Antarctica Res. Ser.*, vol. 75, pp. 203–214, AGU, Washington, D. C.

Karsten, R., H. Jones, and J. Marshall (2002), The role of eddy transfer in setting the stratification and transport of a circumpolar current, *J. Phys. Oceanogr.*, *32*, 39–54.

© 2014. American Geophysical Union. All Rights Reserved.

Kushner, P. J., I. M. Held, and T. L. Delworth (2001), Southern Hemisphere atmospheric circulation response to global warming, *J. Clim.*, *14*, 2238–2249.

Lenaerts, J. T. M., M. R. v. d. Broeke, W. J. v. d. Berg, E. v. Meijgaard, and P. K. Munneke (2012), A new, high-resolution surface mass balance map of Antarctica (1979–2010) based on regional atmospheric climate modeling, *Geophys. Res. Lett*, *39*, L04501, doi:10.1029/2012GL050713.

Marshall, J., and T. Radko (2003), Residual-mean solutions for the Antarctic Circumpolar Current and its associated overturning circulation, *J. Phys. Oceanogr.*, *33*, 2341–2354.

Marshall, J., H. Jones, R. Karsten, and R. Wardle (2001), Can eddies set ocean stratification?, *J. Phys. Oceanogr.*, *32*, 26–38.

McPhee, M., A. Proshutinsky, J. Morison, M. Steele, and M. Alkire (2009), Rapid change in freshwater content of the Arctic Ocean, *Geophys. Res. Lett.*, *36*, L10602, doi:10.1029/2009GL037525.

Melvold, K., J. O. Hagen, J. F. Pinglot, and N. Gundestrup (1998), Large scale variation in accumulation rate in Jutulstraumen ice stream, Dronning Maud Land, Antarctica, *Ann. Glaciol.*, *9*, 231–238.

Munday, D. R., H. L. Johnson, and D. P. Marshall (2013), Eddy saturation of equilibrated circumpolar currents, *J. Phys. Oceanogr.*, *43*, 507–532.

Nicholls, K. W., S. Østerhus, K. Makinson, T. Gammelsrød, and E. Fahrbach (2009), Ice-ocean processes over the continental shelf of the southern Weddell Sea, Antarctica: A review, *Rev. Geophys.*, *47*, RG3003, doi:10.1029/2007RG000250.

Nøst, O. A. (2004), Measurements of ice thickness and seabed topography under the Fimbul Ice Shelf, Dronning Maud Land, Antarctica, *J. Geophys. Res.*, *109*, C10010, doi:10.1029/2004JC002277.

Nøst, O. A., M. Biuw, V. Tverberg, C. Lydersen, T. Hattermann, Q. Zhou, L. H. Smedsrud, and K. M. Kovacs (2011), Eddy overturning of the Antarctic Slope Front controls glacial melting in the Eastern Weddell Sea, *J. Geophys. Res.*, *116*, C11014, doi:10.1029/2011JC006965.

Nunez-Riboni, I., and E. Fahrbach (2009), Seasonal variability of the Antarctic Coastal Current and its driving mechanism in the Weddell Sea, *Deep Sea Res., Part II*, *56*, 1927–1941.

Ohshima, K. I., T. Takizawa, S. Ushio, and T. Kawamura (1996), Seasonal variations of the Antarctic coastal ocean in the vicinity of Lützow-Holm Bay, *J. Geophys. Res.*, *101*, 20,617–20,628.

Rignot, E., S. Jacobs, J. Mouginot, and B. Scheuchl (2013), Ice Shelf melting around Antarctica, *Science*, *341*, 266–270.

Shchepetkin, A. F., and J. C. McWilliams (2005), The regional ocean modeling system (roms): A split-explicit, free-surface, topography-following coordinates ocean model, *Ocean Modell.*, *9*, 347–404.

Smedsrud, L. H., A. Jenkins, D. M. Holland, and O. A. Nøst (2006), Modeling ocean processes below Fimbulisen, Antarctica, *J. Geophys. Res.*, *111*, C01007, doi:10.1029/2005JC002915.

Sverdrup, H. U. (1953), The currents off the coast of Queen Maud Land, *Norsk Geogr. Tidsskrift*, *14*, 239–249.

Timmermann, R., et al. (2010), A consistent data set of Antarctic ice sheet topography, cavity geometry, and global bathymetry, *Earth Syst. Sci. Data*, *2*, 261–273.

Visbeck, M., J. Marshall, T. Haine, and M. Spall (1997), Specification of eddy transfer coefficients in coarse-resolution ocean circulation models, *J. Phys. Oceanogr.*, *27*, 381–402.

Worby, A., C. Geiger, M. Paget, M. V. Woert, S. Ackley, and T. L. DeLiberty (2008), Thickness distribution of Antarctic sea ice, *J. Geophys. Res.*, *113*, C05S92, doi:10.1029/2007JC004254.

© 2014. American Geophysical Union. All Rights Reserved.